Available online at www.sciencedirect.com
SCIENCE DIRECT
Journal of Power Sources 144 (2005) 152–164
JOURNAL OF POWER SOURCES
www.elsevier.com/locate/jpowsour

Effect of load transients on SOFC operation—current reversal on loss of load

Randall S. Gemmen *, Christopher D. Johnson

National Energy Technology Laboratory/DOE, 3610 Collins Ferry Rd., Morgantown, WV 26507, USA

Accepted 27 December 2004
Available online 16 February 2005

Abstract

The dynamics of solid oxide fuel cell (SOFC) operation have been considered previously, but mainly through the use of one-dimensional codes applied to co-flow fuel cell systems. In this paper several geometries are considered, including cross-flow, co-flow, and counter-flow. The details of the model are provided, and the model is compared with some initial experimental data. For parameters typical of SOFC operation, a variety of transient cases are investigated, including representative load increase and decrease and system shutdown. Of particular note for large load decrease conditions (e.g., shutdown) is the occurrence of reverse current over significant portions of the cell, starting from the moment of load loss up to the point where equilibrated conditions again provide positive current. Consideration is given as to when such reverse current conditions might most significantly impact the reliability of the cell.
Published by Elsevier B.V.

Keywords: Fuel cell; Transient; SOFC; Reverse; Loading

1. Introduction

Development of fuel cell systems is being heavily pursued to help provide society's future energy needs. Thus far there have been many demonstrations for a variety of fuel cell technologies, and some units are now commercial. Currently the U.S. Department of Energy is sponsoring the development of solid oxide fuel cell technology through its Solid State Energy Conversion Alliance (SECA) Program. This program focuses on solid oxide fuel cell (SOFC) technology with power output between 3 and 10 kW and having designs suitable for low cost mass production [1]. Enabling mass production capability for fuel cell technology will help to reduce their present high capital cost (~$ 5000 kW^{-1}) to less than $ 400 kW^{-1}, making them economically competitive with other distributed power generation methods. In addition, because of their superior emissions performance, the environmental permit process is expected to be relatively easy. As a result, they can be readily applied for such applications as grid-support [2].

Most of the focus in the development of fuel cell technology has been on achieving good steady state performance. Good performance includes not only good fuel to electric conversion efficiency, but also long lifetime (e.g., >40,000 h for stationary applications). While good steady state performance is critical for the commercialization of fuel cell technology, so also is dynamic performance. Given that real-world applications will incur frequent load changes, particularly at the low power application range (~3–30 kW), systems targeting such applications will likely need to have load-following capability if they are to be commercially viable. Numerous investigators have examined the overall performance of fuel cell systems, and some have examined system dynamics due to load changes, e.g. [3–7]. However, at least for SOFC technology, very little has yet been done to examine what occurs within the cell/stack due to load variations [8–10]. One reason for the lack of work in this area relates to the difficulty of experimentally accessing the in-

* Corresponding author. Tel.: +1 304 285 4536; fax: +1 304 285 4403.
E-mail addresses: randall.gemmen@netl.doe.gov, christopher.johnson@netl.doe.gov (R.S. Gemmen).

0378-7753/$ – see front matter. Published by Elsevier B.V.
doi:10.1016/j.jpowsour.2004.12.027

Nomenclature

A	area at the inlet/outlet of the control volume (m^2)
A_a	electrochemical active area of the control volume (m^2)
C_i	molar concentration of species i ($kg\,mol\,m^{-3}$)
C_{i0}	molar concentration of species i in the freestream
E	specific energy ($J\,kg^{-1}$); Nernst voltage (V)
$\dot{E}$	rate of energy across control surface due to electrochemical reaction
E_{cell}	operating cell voltage (V)
F	Faraday's constant (96,485 C g mol^{-1} electrons)
F_s	control volume surface frictional force (N)
G	Gibbs free energy
h	flow channel height
i	current density ($A\,cm^{-2}$)
i_0	exchange current density ($A\,cm^{-2}$)
i_L	diffusion limiting current density
L_A	voltage loss due to electrochemical reaction (V)
L_C	voltage loss due to concentration losses resulting from diffusion of reactants (V)
L_R	voltage loss due to ionic/electronic resistive media (V)
M	momentum within control volume ($kg\,m^2\,s^{-1}$)
$\dot{M}$	rate of momentum flow across a control surface ($kg\,m\,s^{-2}$)
n	number of participating electrons in fundamental electrochemical reaction
N_i	molar flow rate of species i (in/out of control volume) ($kg\,mol\,s^{-1}$)
P	pressure at the inlet/outlet of the control volume (Pa)
P'	net rate of flow energy added at control volume inlet and outlet. Zero for exit control volume where enthalpy is directly used in the conservation equation
Q_s	net boundary heat addition (W)
R	net resistance of cell ($=R_o + R_c$) ($\Omega\,m^2$)
R_o	ohmic resistance of the cell ($\Omega\,m^2$)
R_c	contact resistance between cell conductive layers ($\Omega\,m^2$)
R_i	molar source of species i due to electrochemical reaction ($kg\,mol\,s^{-1}$)
R_u	universal gas constant
S	supply flow rate
ΔS	entropy generated per mole of reactant ($J\,g\,mol^{-1}\,K^{-1}$)
t	material thickness
T	temperature (K)
v	velocity ($m\,s^{-1}$)
V	finite control volume (m^3)
w	mass flow ($kg\,s^{-1}$)
y	mole fraction

Greek symbols

α	electrochemical transfer coefficient [1]
η	electrochemical overpotential (V)
ρ	density ($kg\,m^{-3}$)

Subscripts and superscripts

a	fuel electrode (anode for $i > 0\,A\,cm^{-2}$)
Air	air
c	air electrode (cathode for $i > 0\,A\,cm^{-2}$)
e	electrode
H_2	hydrogen
i	species index

ternal features of a cell/stack without modifying the flow and temperature which are critical to determining the cell performance.

At the National Energy Technology Laboratory (NETL), work is underway to examine cell and stack dynamic performance. Both models and experimental work are being pursued. Experimentally, we have been studying the 'random' fluctuations that occur in PEM fuel cells when heavily loaded and methods for reducing such fluctuations in order to extend the operating range of a fuel cell [11]. This paper reports on modeling efforts related to SOFC cell/stack performance under transient loads. Three planar geometries are considered: co-flow, cross-flow, and counter-flow (CoF, CrF, CtF, respectively). In the following section, a detailed description is given of the model tool developed at NETL for dynamic fuel cell analysis. One previous application of this tool has been in the study of the dynamic performance of hybrid systems [3,12]. In Section 4, discussion of how the model is applied to investigate the load transient characteristics of an SOFC is made. Next, results are given, and following which a detailed analysis of the results is presented. Finally, conclusions from the present work are made, along with suggestions for future work.

2. Model description

In the present discussion, a generic bi-polar, planar fuel cell is examined, see Fig. 1. Straight, single pass flow channels are assumed to distribute fuel and oxidant to the fuel electrode and air electrode sides of the cell, respectively. (We avoid the terms anode and cathode for reasons that will be understood later.) As described in detail below, various submodels can be employed for analyzing the conditions within these channels depending on the requirements of the model application to resolve various time scales. Regardless of flow geometry, CoF, CrF, or CtF, these flow channels can be analyzed using one-dimensional flow calculations to provide

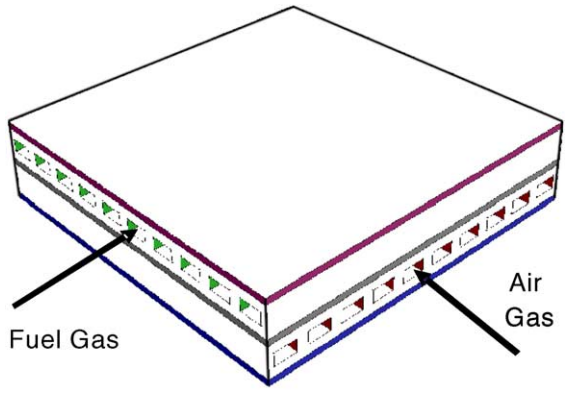

Fig. 1. Planar cross-flow cell geometry.

useful design information. While CoF and CtF geometries can be analyzed using single channels for the fuel and air, the cross-flow model must be analyzed using an assembly of one-dimensional flow channels [13]. The justification for using one-dimensional flow calculations can also be found from an analysis of the characteristic time scales present in a fuel cell.

2.1. Characteristic time scales

A first-order analysis provides estimates for the various time scales occurring in SOFC systems. Results from such an analysis are given in Table 1. The analysis assumes an anode supported SOFC fuel cell having cell parameters shown in the last column of Table 3. The first column in Table 1 is the name of a particular process time scale. Associated with each process is its rate and capacity parameters, and equations are provided in the table for each value. Here, ρ is the density (mass or mol), A_x the flow passage cross-section, V the flow passage volume, V_c the cell voltage, A_c the active area, D the molecular diffusion coefficient, C_p the specific heat, C the electric or thermal capacity, t the electrode thickness, L the cell length, and V the gas velocity. The ratio of the capacity and rate values provide the first-order estimate of the time scale for each process. Because some transport processes depend on a characteristic length scale (e.g., diffusion), and because there are several distinct characteristic length scales within a fuel cell (electrode thickness, cell length, etc.), numerous transient time scales are present for the same fundamental transport mechanism.

Table 1
Characteristic transient time scales of a planar SOFC

Time scale name	Process rate parameter		Capacity parameter		Time scale, τ (s)
	Name	Value	Name	Value	
A. Cell charging time	Current density (I/A_c)	10^4 A m^{-2}	Double-layer capacity (CV_c)	10^{-1} C m^{-2}	10^{-5}
B. Cathode gas electrode mass diffusion time	Molecular diffusion rate ($\rho DA_c/t$)	10^{-1} mol s^{-1}	Cathode electrode mole capacity (ρtA_c)	10^{-6} mol	10^{-5}
C. Anode gas electrode mass diffusion time	Molecular diffusion rate ($\rho DA_c/t$)	10^{-1} mol s^{-1}	Anode electrode mole capacity (ρtA_c)	10^{-4} mol	10^{-3}
D. Cathode electrode thermal diffusion time	Thermal diffusion rate (kA_c/t)	10^3 J s^{-1} K^{-1}	Cathode electrode thermal capacity ($\rho C_p tA_c$)	10^0 J K^{-1}	10^{-3}
E. Convective transport time	Specific gas volume flow rate (V/A_x)	10^0 m s^{-1}	Specific gas volume (V/A_x)	10^{-1} m	0^{-1}
F. Cell Reactant consumption time	Faradaic mole density ($I/(nFA_c)$)	10^{-2} mol (s m^2)$^{-1}$	Specific mole density ($\rho h/MW$)	10^{-2} mol m^{-2}	10^0
G.Anode gas streamwise mass diffusion time	Molecular diffusion rate ($\rho DA_x/L$)	10^{-5} mol s^{-1}	Anode cell mole capacity (ρLA_x)	10^{-4} mol	10^1
H. Anode gas streamwise thermal diffusion time	Thermal diffusion rate (kA_x/L)	10^{-4} J s^{-1} K^{-1}	Anode-gas thermal capacity ($\rho C_p LA_x$)	10^{-3} J K^{-1}	10^1
I. Cathode gas streamwise thermal diffusion time	Thermal diffusion rate (kA_x/L)	10^{-4} J s^{-1} K^{-1}	Cathode gas thermal capacity ($\rho C_p LA_x$)	10^{-3} J K^{-1}	10^1
J. Anode electrode thermal diffusion time	Thermal diffusion rate (kA_c/t)	10^1 J s^{-1} K^{-1}	Anode electrode thermal capacity ($\rho C_p tA_c$)	10^1 J K^{-1}	10^1
K. Cathode gas streamwise mass diffusion time	Molecular diffusion rate ($\rho DA_x/L$)	10^{-5} mol s^{-1}	Cathode cell mole capacity (ρLA_x)	10^{-4} mol	10^1
L. Cell heating time	Gas heat transfer rate (hA_c)	10^{-2} J s^{-1} K^{-1}	Cell heat capacity (ρCtA_c)	10^1 J K^{-1}	10^3
M. Anode electrode streamwise thermal diffusion time	Thermal diffusion rate (kA_x/L)	10^{-2} J s^{-1} K^{-1}	Anode electrode thermal capacity ($\rho \mathrm{CLA_x}$)	10^1 J K^{-1}	10^3
N. Cathode electrode streamwise thermal diffusion time	Thermal diffusion rate (kA_x/L)	10^{-4} J s^{-1} K^{-1}	Cathode electrode thermal capacity ($\rho \mathrm{CLA_x}$)	10^0 J K^{-1}	10^4

The results of Table 1 show a wide range of time scales (10^{-5} to 10^{4} s) spanning over nine orders of magnitude. These results can be helpful to guide engineering analysis by showing how transport models can be simplified, and yet still accurately predict a given fuel cell performance parameter. In general, to allow for efficient use of computational time, it is customary in modeling to only consider the details of a given transport process if its characteristic time scale is within one or two orders of magnitude from the principle effect being examined. Hence, if one is investigating load-following characteristics of a fuel cell at a time scale on the order of 10^{-2} s, then any transport process having a characteristic time greater than 10^{0} s can be assumed constant over durations much less than 10^{0} s; hence, no detailed model equation is necessary to relate the parameters of the transport process to the rest of the model. On the other hand, if there is a transport process having a characteristic time scale less than 10^{-4} s, then the related physical parameters can be assumed to behave quasi-steady. Here, a steady state equation is required to relate the parameters of the transport process to the rest of the model.

As an example of time scale analysis, consider the case of a fuel cell transient over the duration of 100 s with a resolution of 1 s. Examination of the streamwise convection and diffusion in Table 1, two independent transport mechanisms that control streamwise species distribution, shows that the time scale for convective transport is 10^{-1} s while the time scale for streamwise diffusion is 10^{1} s. Because the convective response is much faster than the desired resolution, the *gas flow* can be considered quasi-steady. Also, it controls the reactant distribution much more strongly than diffusion, allowing us to ignore streamwise diffusion for most analyses of this given type of fuel cell geometry. Additionally, the time scale for transverse diffusion over the channel is less than 10^{-3} s. Because this is much faster than the convective time scale, the reactants in a channel can be considered largely uniform in the transverse direction. The ability to ignore these (and other) transport mechanisms helps to speed computational predictions making engineering analysis more efficient by allowing the use of one-dimensional quasi-steady gas models, Fig. 2.

The only time the above method fails is if the principle effect being studied is highly sensitive to a given transport process. Such conditions occur, for example, in the analysis of combustion (e.g., the post-oxidizer of a fuel cell) where chemical reactions, having time scales on the order of 10^{-3} to 10^{-5} s, occur (autothermally) in a heated mixture of fuel and air. For these problems one often sees that the spatial distribution of the reaction (governed by convection time scale of 10^{0} s) significantly depends on the reactions that evolve at time scales on the order of 10^{-5} s. In fuel cell electrochemistry, however, the chemical reactions are 'constrained' by the external control of the current load, something that offers a significant advantage over analysis in combustion chemistry.

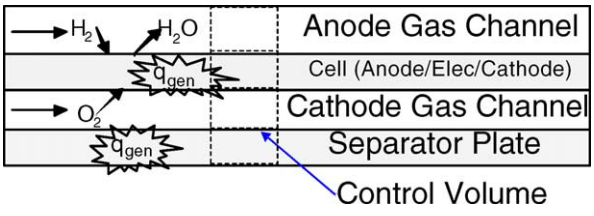

Fig. 2. Example of planar co-flow cell geometry. Other geometries employ similar to 1D gas analysis.

The present paper investigates two domains of transient performance, and the above characteristic time scale results are used to guide the development of a proper model. The first domain of investigation examines the ability of the model to capture the fast transient current loading behavior of a small 'button' fuel cell down to a resolution of about 0.005 s. The second domain of investigation applies the model to a full cell (10 cm × 10 cm), and is used to predict the transient performance of the fuel cell at a resolution of about 10 s following a load change. Hence, the former investigation will include electrode diffusion effects, while the latter investigation will limit its consideration to the thermal response and treat the gas phase as quasi-steady. Both cases will follow the quasi-steady electrochemical response that results from their respective load changes.

2.2. Model assumptions

The analysis considers the behavior of a single unit cell located within an infinite series of cells undergoing the same dynamics. Hence, the overall thickness of the unit cell (separator plate to separator plate (also called interconnect plate)) is a symmetry length, and for computational efficiency, is the only length that needs to be resolved. Here, the term cell is used to describe the lumped fuel electrode and air electrode together with the electrolyte material.

Key assumptions of the model are:

1. One-dimensional behavior along the streamwise direction of all gas channels.
2. In-plane heat conduction can be neglected—an order-of-magnitude analysis for the Peclet number (ratio of in-plane convective transport to solid conduction) shows that convection in the gas channels are 4–10 times larger than conduction, even for composite nickel fuel electrode supported geometries having conductivity of $\sim$6.2 W m^{-1} K^{-1} [14].
3. Ideal gas behavior with variable specific heats.
4. Lumped temperature for the cell and separator plates along the transverse direction due to low Biot number of the cell convection ($Bi = ht/k = \tau_J/\tau_L$ in Table 1).
5. Gas-to-solid heat transfer is by convection. Radiation is ignored at this time, but in general can be important.
6. There is no carbon deposition.
7. No gas phase reactions occur.
8. Fuel electrode electrochemical activation overpotential is negligible [15].
9. The fuel cell has 100% current efficiency—all reactants generate their ideal number of electrons.

Table 2
Fundamental one-dimensional dynamic equations for an ideal gas

$A\frac{\partial C_k}{\partial t} + \frac{\partial C_k v_x}{\partial x} = -R'_{sk}$	(F1)
$\rho A\frac{\mathrm{D}v_x}{\mathrm{D}t} = F_x - A\frac{\partial P}{\partial x} - M_b$	(F2)
$\rho A\frac{\mathrm{D}h}{\mathrm{D}t} - A\frac{\mathrm{D}P}{\mathrm{D}t} = Q_s + F_L - E_b$	(F3a)
$\rho A\frac{\mathrm{D}u}{\mathrm{D}t} = Q_s + F_L + E_b$	(F3b)

Primarily due to assumption 6 above, the model to be presented is most accurate for fuel electrode conditions having $H_2 + H_2O$ with little or no carbon species. This is acceptable for the present work given that the goal is to provide a 'first-look' at some of the unsteady performance results that can occur in SOFC systems.

2.3. Gas phase equations

The fundamental dynamic equations required for solution of the one-dimensional flow in a fuel cell are listed in Table 2. Here, the total derivative, D/Dt includes only the convective transport in the 'x' direction, as shown explicitly for Eq. (F1). Eqs. (F1), (F2), (F3a) and (F3b) describe the conservation of species, momentum, and thermal energy, respectively [16]. In Table 2, A is the flow area of the one-dimensional passage, C_k and R_{sk} are the mole density and net surface mole supply rate (mol (x-unit distance)$^{-1}$) of species k, respectively, v_x the velocity in the x-direction, P the pressure, M_b the momentum lost at the surface due to flow at the boundaries, ρ the mass density, F_x the net shear force in the x-direction on the side surfaces of the elemental control volume, F_L the thermal energy generated due to fluid shear force, h the enthalpy, E_b the enthalpy addition due to flow at the side boundaries, and Q_s the surface heat into the elemental control volume.

Multiplying the left- and right-hand sides of Eq. (F2) by v and adding (F3a) and (F3b) results in an equation for the conservation of total (thermal and mechanical) energy. Taking these latter equations and Eqs. (F1) and (F2) and integrating over the x-direction of a single control volume (Fig. 2) results in the following set of dynamic equations to be solved for each finite control volume that is present in a one-dimensional array of control volumes (see also [4]). For species conservation:

$$V\frac{\mathrm{d}C_i}{\mathrm{d}t} = N_{i_{\mathrm{inlet}}} - N_{i_{\mathrm{exit}}} + R_k \tag{1}$$

For momentum conservation:

$$V\frac{\mathrm{d}\rho v}{\mathrm{d}t} = \dot{M}_{\mathrm{inlet}} - \dot{M}_{\mathrm{exit}} - \dot{M}_{\mathrm{R}} + P_{\mathrm{inlet}}A_{\mathrm{inlet}} - P_{\mathrm{exit}}A_{\mathrm{exit}} + F_s \tag{2}$$

For total energy conservation:

$$V\frac{\mathrm{d}\rho E}{\mathrm{d}t} = w_{\mathrm{inlet}}E_{\mathrm{inlet}} - w_{\mathrm{exit}}E_{\mathrm{exit}} + \dot{E}_{\mathrm{R}} + Q_s + P' \tag{3}$$

Definitions for the various parameters are given in nomenclature. The subscripts 'inlet' and 'exit' denote the left and right surfaces of the control volume. The molar source of species k for a given control volume, R_k, arises from the electrochemistry occurring at the surface of the electrolyte. Under normal fuel cell operation ($i > 0\ \mathrm{A\,cm^{-2}}$), the electrochemistry consumes O_2 on the *air electrode* and H_2 on the *fuel electrode*, and produces H_2O on the *fuel electrode*.[1] Under reverse fuel cell operation (electrolysis mode, $i < 0\ \mathrm{A\,cm^{-2}}$), the electrochemistry produces O_2 on the *air electrode* and H_2 on the *fuel electrode* and consumes H_2O on *the fuel electrode*. These sources R_k, are directly related to the electric current according to the number of electrons, n_k, associated with each

Table 3
Cell data and operating conditions

Parameter	Unit	Value (button cell)	Value (planar cell)
Fuel electrode specification			
Height of flow channel, h	mm	–	1.0
Electrode thickness, t_e	mm	1.025	1.0
Porosity/tortuosity	–	See text	0.11
Temperature, T	K	1073	1023
Pressure, P	Pa	101100	Same
Supply H_2 mole fraction	–	0.85	0.54
Supply H_2O mole fraction	–	0.15	0.16
Supply CO_2 mole fraction	–	–	0.30
Electrode heat capacity, C_p	$\mathrm{J\,kg^{-1}\,K^{-1}}$	640	Same
Electrode density, ρ	$\mathrm{kg\,m^{-3}}$	4200	Same
H_2 supply, S_{H_2}	slpm	0.050	1.2
Air electrode specification			
Height of flow channel, h	mm	–	2.0
Electrode thickness, t_e	μm	68	50
Porosity/tortuosity	–	See text	0.11
Active area	$\mathrm{cm^2}$	2.19	100
Inlet temperature, T	K	1073	1023
Pressure, P	Pa	101100	Same
Supply O_2 mole fraction	–	0.204	0.21
Supply N_2 mole fraction	–0.766	0.79	
Supply H_2O mole fraction	–	0.03	0.0
Electrode heat capacity, C_p	$\mathrm{J\,kg^{-1}\,K^{-1}}$	570	Same
Electrode density, ρ	$\mathrm{kg\,m^{-3}}$	3300	Same
Exchange current density, i_0	$\mathrm{A\,m^{-2}}$	285	3250
Transfer coefficient, α	–	0.5	0.5
Air supply, S_{Air}	slpm	1.0	5.5
Electrolyte specification			
Electrolyte thickness, t	μm	7	5
Electrolyte heat capacity, C_p	$\mathrm{J\,kg^{-1}\,K^{-1}}$	600	Same
Electrolyte density, ρ	$\mathrm{kg\,m^{-3}}$	5100	Same
Separator specification			
Thickness, t	mm	NA	0.7
Separator heat capacity, C_p	$\mathrm{J\,kg^{-1}\,K^{-1}}$	NA	450
Separator density, ρ	$\mathrm{kg\,m^{-3}}$	NA	8900
Cell specification			
Contact resistance, R_c	$\Omega\,\mathrm{cm^2}$	0.04	0.06
Ohmic resistance, R_o	$\Omega\,\mathrm{cm^2}$	0.105	0.10

[1] Because this paper examines conditions of both *normal* and *reverse* fuel cell operation modes, the terms 'cathode' and 'anode' become confused, since depending on the mode of operation they will apply to opposite electrodes. Instead, the paper will use the terms 'air electrode' and 'fuel electrode' to represent the electrodes where O_2 and $H_2 + H_2O$ exist, respectively.

specie molecule consumed/generated in the electrochemical process. For the present analysis on solid oxide cells, four electrons are processed by each oxygen molecule consumed at the air electrode, and two electrons are processed by each hydrogen (and water vapor) molecule processed at the fuel electrode. Explicitly, we have

$$R_k = \frac{A_a i}{n_k F} \tag{4}$$

n_k for O_2, H_2, and H_2O, are -4, -2, and 2, respectively. Hence, for $i < 0\ \mathrm{A\,cm^{-2}}$, $R_{O_2} > 0\ \mathrm{kg\,mol\,s^{-1}}$.

In Eq. (2), the momentum flow, $\dot{M}_R$, comes from the term M_b in (F2) and is the net momentum loss resulting from reactant removal out of the control volume at the electrolyte surface due to the electrochemical reaction. For mass addition at the electrolyte surface, it is assumed that no net addition of momentum occurs—that is, there is no favored direction to the emission of molecules from the electrolyte due to electrochemical reactions, and hence no net momentum is produced.

The parameter, $\dot{E}_R$, in Eq. (3) is an energy flow term that resulted from E_b in Eqs. (F3). $\dot{E}_R$ represents the net enthalpy added to the control volume resulting from species emission/absorption at the electrolyte surface due to the electrochemical reaction. Here, the energy of the species removed from the gas phase is assessed at the temperature of the gas, and the energy of the species added to the gas phase is assessed at the temperature of the cell.

For all control volumes except at the exit, E is the sum of internal energy and kinetic energy. For the exit control volume we assume pressure fluctuations are zero (constant pressure boundary condition), and the enthalpy plus kinetic energy is used. The assumption here is that the exit of the fuel cell goes to near atmospheric conditions (or some other specified fixed exit pressure) which results in a constant pressure boundary condition. On the other hand, the inlet pressure can vary with time as may be caused by the action of an upstream flow controller.

The model allows for two types of gas phase solutions. One is fully dynamic in that it solves the above one-dimensional dynamic equations for species, momentum and energy. The other assumes quasi-steady gas phase conditions to exist and solves the steady-state gas phase equations for these parameters given the instantaneous conditions at its boundaries. Here, the same equations listed above are used, but the time-derivative terms are dropped and the resulting algebraic equations are solved simultaneously. Since flow times for gases through a cell are on the order of 1 s or less (see Table 1), the quasi-steady solution is useful to speed up calculations on long transients (e.g., >10 s).

2.4. Solid phase energy equation

For control volumes present in the cell and separator plate, an energy equation similar to Eq. (3) arises, but the convective terms will obviously be zero. Also, for any solid, there is an additional energy source term due to internal ohmic heating. For the cell alone, there is a final additional energy generation term due to the overall reaction of H_2 with O_2. This energy generation results from the reaction process which experiences a net change in entropy [17]:

$$Q_{rxn} = -\frac{T\,\Delta S\,A_a i}{nF} \tag{5}$$

where ΔS is the change in entropy (per mole of H_2) of the overall reaction of H_2 with O_2, $A_a i$ the current through the control volume, n (no subscript) the number of electrons processed per mole of H_2, and F the Faraday constant. Hence, the following equations apply to the cell and separator plate, respectively:

$$V\frac{\mathrm{d}\rho E}{\mathrm{d}t} = \dot{E}_R + Q_s + Q_{rxn} + iR \tag{6}$$

$$V\frac{\mathrm{d}\rho E}{\mathrm{d}t} = Q_s + iR \tag{7}$$

where E is the internal energy of the given solid material, $\dot{E}_R$ the net enthalpy added to the cell resulting from species emission/absorption for both fuel electrode and air electrode surfaces, Q_s the same as before, and R the cell net electronic + ionic + contact cell resistance ($\Omega\,\mathrm{m^2}$).

2.5. Cell voltage and loss mechanisms

The cell voltage is modeled by accounting for various loss mechanisms in an otherwise ideal cell. The ideal fuel cell voltage is given by

$$E_N = -\frac{\Delta G}{nF} \tag{8}$$

ΔG is the change in Gibbs free energy for reaction of H_2 with O_2 at the temperature and pressure of the cell, which provides the maximum available work energy for this reaction. If this work energy is given to n number of electrons, then their voltage would be E_N.

Voltage losses (overpotentials) within a fuel cell result from three primary effects: (1) electrical and ionic resistance, L_R; (2) change in electrolyte surface reactant concentrations from their free-stream values due to diffusion transport through the electrodes, L_{Ci}; and (3) an activation overpotential needed to drive the electrochemical reactions, L_A [18]. As shown below, these losses depend on current flow through the cell. The cell voltage under current loading can be defined as

$$E_{cell} = E_N - L_R - \sum L_{Ci} - L_A \tag{9}$$

This cell voltage is the voltage that would exist on some external load that draws current from the cell.

The net cell electronic + ionic + contact resistive losses are modeled as

$$L_R = Ri \tag{10}$$

where i is the local current density for a given control volume.

For diffusive losses, the model can either employ a bulk quasi-steady diffusion loss mechanism, or resolve the dynamic diffusion through the electrodes for each control volume. The latter model is given in detail by Gemmen et al. [19].

The quasi-steady diffusion loss model uses the following set of equations derived from an analysis of the effect of diffusion on reactant concentrations near the electrolyte/electrode interface and the subsequent loss to the cell Nernst potential. For reactant k diffusion toward the electrolyte interface, the loss is given as

$$L_{Ci} = -\frac{R_u T}{nF} \ln\left(\frac{1-i}{i_{Lk}}\right) \tag{11a}$$

where i_{Lk} is the diffusion limiting current density for reactant k, which is modeled as

$$i_{Lk} = \frac{C_{k0} D_{eff} nF}{t_e} \tag{12a}$$

where D_{eff} is the effective diffusivity for the transported reactant, and t_e the electrode diffusion thickness. (Note that because of the formulation given above, the sign of i_L is always the same as i. This understanding is important when later we discuss conditions for current reversal in a cell, $i < 0$.) For reactant diffusion away from the electrolyte interface, the quasi-steady loss model is

$$L_{Ci} = \frac{R_u T}{nF} \ln\left(1 - \left(\frac{i}{i_{Lk}}\right)\left(1 - \frac{1}{y_{i0}}\right)\right) \tag{11b}$$

where now the limiting current density is given by

$$i_{Lk} = \frac{C_0(1-y_{k0}) D_{eff} nF}{t_e} \tag{12b}$$

For positive current ($i > 0.0$), Eqs. (11a) and (12a) apply to O_2 on the air electrode and H_2 on the fuel electrode, while Eqs. (11b) and (12b) apply to H_2O on the fuel electrode. For negative current, Eqs. (11b) and (12b) apply to O_2 on the air electrode and H_2 on the fuel electrode, while Eqs. (11a) and (12a) apply to H_2O on the fuel electrode.

For the activation loss, L_A, we have

$$L_A = \eta_c + \eta_a \tag{13}$$

As shown in Eq. (13), in general there is an activation loss at both air and fuel electrodes, η_c and η_a, respectively. For the work here, because air electrode losses dominate L_A, the fuel electrode activation is ignored.

Under steady state, the electrochemical loss is often represented using the Butler–Volmer equation [20]:

$$i = i_0\left(\exp\left(\frac{\alpha n F \eta}{R_u T}\right) - \exp\left(\frac{(1-\alpha) n F \eta}{R_u T}\right)\right) \tag{14}$$

Because of a double-layer capacitance at the electrolyte–electrode interface, there is actually a short transient behavior to the activation loss. The transient loss is typically represented as a parallel resistor–capacitance circuit at each electrode, where the resistor represents the electrochemical loss mechanism. The model can be optionally set to solve for the double-layer transient, or to assume fully quasi-steady loss behavior (Eq. (14)). To solve for the transient double-layer capacitance behavior, the model employs the following equation [21]:

$$\frac{d\eta}{dt} = \frac{i_c}{C_{dl}} \tag{15}$$

where i_c is the current density that charges the double-layer capacitance of C_{dl} ($F\,m^{-2}$). A generally recognized value for C_{dl} has not been established, but values as high as $1\,F\,m^{-2}$ have been suggested [21,22]. Because of the parallel R–C circuit, the instantaneous current through a given computational node is the sum of current through both R and C elements. Hence,

$$i_c = i - i_R \tag{16}$$

with the assumption of quasi-steady electrochemical loss, i_R is given by Eq. (14). Because the time scale for the double-layer capacitance is on the order of 100 μs is or less (see Table 1), the present work uses the quasi-steady Butler–Volmer model.

Note that because the fuel and oxidant are consumed as they pass through the cell, the ideal cell voltage at the exit will be lower than that at the inlet. The actual overall cell voltage achieved will approach the lowest achievable voltage due to the high conductivity of the electrode surfaces [18]. As usual for loss mechanisms, it is assumed that the unachieved voltage over the surface is dissipated as heat directly into the cell material.

2.6. Reversible fuel cell operation

The models for the loss terms cited above are common to fuel cell modeling [8]. However, most past modeling efforts simply consider conditions where current flow, i, through the cell is positive. As will be shown below, there are transient conditions where reverse current, $i < 0$, may arise. These conditions arise when E_{cell} is greater than E_N, which means that the loss terms on the right-hand side of Eq. (9) must become positive. (Clearly, to force reverse current, the operating electrical potential must be greater than the chemical (i.e., Nernst) potential.) Because rate limiting processes are present under these conditions just as for positive current conditions, potential losses occur, and using the above models requires these losses to be positive-valued. Given the formulations above, proper numerical treatment for both resistance and activation losses (Eqs. (10) and (14)) occurs automatically for both positive and negative current domains, but for proper accounting of diffusion under negative current conditions, the sign on diffusion terms (L_{Ci}) must be reversed. This can be accommodated by changing Eq. (9) to be

$$E_{cell} = E_N - L_R + \sum L_{Ci} - L_A \tag{17}$$

for negative current conditions.

3. Numeric representation and solution technique

The above equations allow the transient solution of one-dimensional arrays of both gas and solid bodies that comprise a fuel cell. Depending on the needs of the engineer, different submodels can be employed (e.g., resolving the double-layer transient may not be needed for studies looking at the longer time scales associated with cell thermal transients and their impact on cell voltage). Finite control volumes for both gas passages and solid bodies are identified and properly associated to provide proper conservation of mass, momentum and energy. The NETL code that implements the above equations can solve for co-flow, counter-flow, and cross-flow fuel cell geometries. For the cross-flow geometry, an array of fuel electrode channels and air electrode channels are generated and assembled to form such a cell, similar to the work of Ahmed et al. [13]. For the co-flow and counter-flow geometries, only one channel of both fuel electrode and air electrode gas is required.

Any number of control volumes are possible along the streamwise direction for each of the four major components: fuel electrode gas, air electrode gas, cell, and separator plate. For the work reported here, eight control volume 'nodes' are used which provides sufficient resolution to capture fuel cell performance [12]. For solving dynamic gas phase problems, the equations are solved following the techniques outlined by Patankar [23], wherein the pressure and velocity nodes are staggered.

In the solution of the model, either the cell voltage or total cell current is specified by the user (voltage control versus current control). To solve conditions of the cell at every time step based on specified instantaneous boundary conditions, the model first solves for all node electrochemical reaction rates (current densities) given the specified cell voltage or total current. If a quasi-steady activation loss is assumed (i.e., no double-layer dynamics to be solved), then an iterative approach is used to determine the cell current density profile. Node current at each time step is iterated so as to ensure a uniform cell voltage (to within 4 μV). A uniform cell voltage is a common assumption in fuel cell modeling given the high electric conductivity of the electrodes and separator plates. A combination between a Newton and simple bisection method is used to converge to the desired solution. Once the current is known, the dynamic solution for mass, momentum and energy (Eqs. (1)–(3)) for all cell domains is determined through an explicit first-order backward Euler method. For a quasi-steady gas solution, the conservation equations for mass, momentum, and energy are solved simultaneously in a coupled fashion with the electrochemical solution.

4. Model application

The model has been tested for self-consistency regarding the application of its various submodels. For example, the quasi-steady gas solution was tested and found to provide the same conditions as the fully dynamic gas model predictions when taken to steady state. The dynamic model was also verified by comparing its results to that of the National Fuel Cell Research Center and found to be comparable [24].

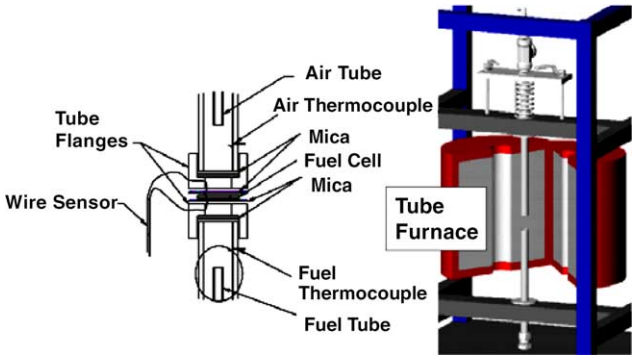

Fig. 3. Experimental hardware.

The model was also tested in cross-flow geometry by comparing results to that of Ahmed et al. [13]—the results were the same to within 4%. In the present work, we report the success of model validation using experimental cell transient data. The cell transient data was obtained from a button cell operated inside an enclosed rig that controlled both the flow of air and fuel. A view of the test set up is shown in Fig. 3.

Finally, the model was applied to investigate three cases of planar 10 cm × 10 cm fuel cell design (CoF, CrF and CtF). For each case, several load transients were imposed that are representative of real world applications where a system might experience anything from small changes in load (<30%) to complete load loss. For simplicity, following the work of Ahmed et al. [13], eight channels for fuel electrode flow and eight channels for air electrode flow are considered using the same one-dimensional model described above for each channel.

4.1. Button cell study

For the transient button cell cases, a fully dynamic gas solution was calculated using the electrode diffusion model of Gemmen et al. [19], but the double-layer transient was ignored (which again has a time constant on the order of 100 μs and is very short relative to the transient under study). Given the uniformity of the conditions over the cell that can be expected from the known flow conditions used in the experiment, the model uses a single control volume for the fuel electrode and air electrode systems. The region up to 3 cm from the surface of the cell was included in the model analysis. Load perturbation occurred through current control.

Values for the model parameters used in the button cell comparisons are shown in Table 1. The values for the parameters were determined from the cell specifications given by the University of Utah from where the cells were obtained, and from the known conditions of the test fixture. The actual button cell included thin fuel electrode and air electrode interlayers, 25 and 18 μm, respectively, and these thicknesses were incorporated into the bulk electrode to establish a single

Fuel Inlet	Air Inlet							
	1	9	17	25	33	41	49	57
	2	10	18	26	34	42	50	58
	3	11	19	27	35	43	51	59
	4	12	20	28	36	44	52	60
	5	13	21	29	37	45	53	61
	6	14	22	30	38	46	54	62
	7	15	23	31	39	47	55	63
	8	16	24	32	40	48	56	64

Fig. 4. Model node ID numbers used on charts.

electrode for the model. This assumption should be reasonable given the relatively thin nature of these layers. The contact resistance value shown (obtained by matching the experimental VI data) was attributed to the experimental method used to contact the fuel electrode and air electrode current leads to the button cell.

4.2. Planar cell cases

For the three CoF, CrF and CtF transient studies, the quasi-steady gas and activation loss models were used together with the bulk diffusion model, and the model was used to predict the response of the cell to load transients. This study employed voltage controlled transients. The model parameters used for these studies are also shown in Table 3. These parameter values provide cell performance close to what is anticipated for SECA Program fuel cell systems—at a cell voltage of 0.77 V and fuel and air utilizations of 0.81 and 0.11, respectively, cell average current density ~0.74 A cm^{-2}. The cells were assumed to have a 10 cm × 10 cm active area, so the channel lengths for both fuel electrode and air electrode are 10 cm long. As mentioned previously, eight channels are used for both the fuel electrode and air electrode, and each channel has eight nodes. The resultant size of each node is 12.5 mm × 12.5 mm. For reference, the node (control volume) ID numbers for the model are shown in Fig. 4. Time steps used in the solution of the model ranged from 3.0E−2 to 8.0E−2 s, which were controlled by the solution of the solid phase thermal transient (the gas was assumed quasi-steady).

5. Results

Results for the button cell and 10 cm × 10 cm cell cases are now presented.

5.1. Button cell case

Transient button cell experimental and model results are shown in Fig. 5. Two load changes were examined, one with load reduced from 1 to 0 A, the other from 2 to 0 A. For each case, the data was taken at both a short time (fast data speed) and a long time (slow data speed) in order to capture

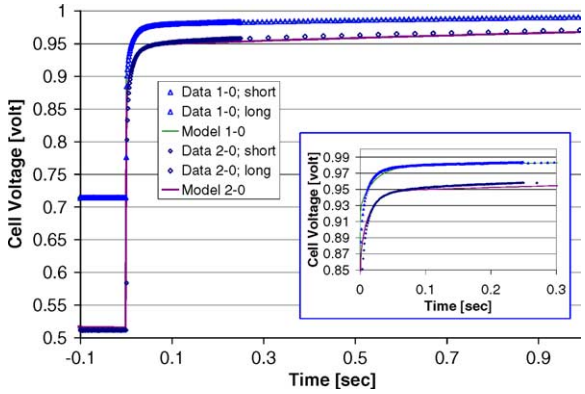

Fig. 5. Transient button cell data and model comparison. Inset shows same data over shorter time scale.

the transient as closely and fully as possible. As can be seen, the two sections of the transient data align very well, indicating good repeatability of the experimental data. Results for the 1 A load change employed a porosity/tortuosity value of 0.025, while the 2 A load change employed a value of 0.020. These were selected to best fit the data. The model results agree fairly well with the experimental data, which provides some measure of confidence in the model.

5.2. Cross-flow case—load increase

Results from the cross-flow study examining load increase dynamics are shown in Figs. 6 and 7. Fig. 6 shows transient current densities at several node locations on the cell for a 0.96–0.84 V load change case—see Fig. 4 for a key to the node ID numbers. As can be seen, there is an initially high current flow through the cell, and then as the temperature of the cell slowly increases due to internal heating, the Nernst voltage gradually drops which causes a slow drop in current flow. It is also seen that while the cathode inlet and exit nodes show fairly similar current density before and initially after the load change, once the cell has reached its new equilibrium following the load change, the inlet and exit nodes are significantly different. Finally, it is seen that an overall increase in current by a factor of about 3.75 results from this load change.

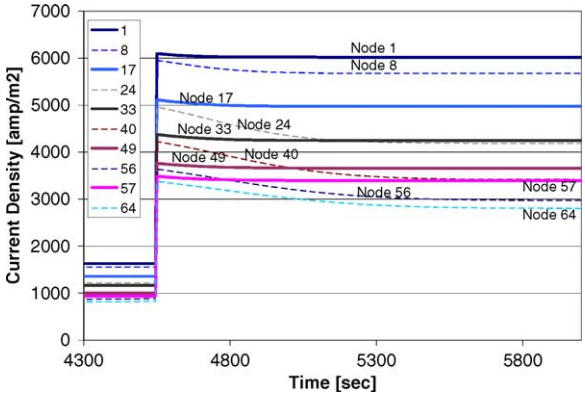

Fig. 6. Cross-flow load increase (0.96–0.84 V).

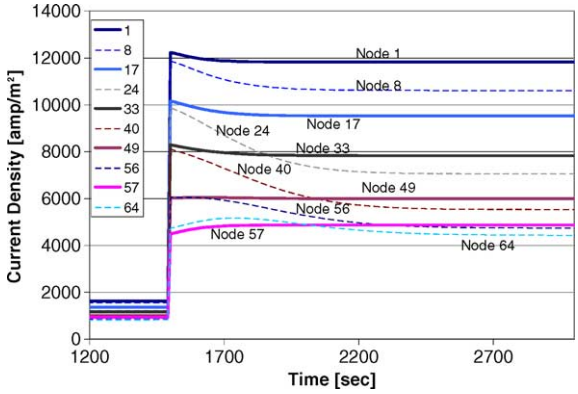

Fig. 7. Cross-flow load increase (0.96–0.70 V).

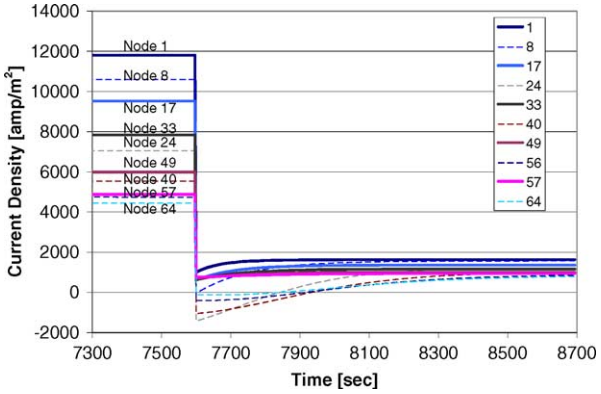

Fig. 9. Cross-flow load decrease (0.70–0.96 V).

Fig. 7 shows similar results as in Fig. 6 but for a larger 0.96–0.70 V load change. For this transient, there is an overall current increase by a factor of about 6.6. While most of the results highlighted for the prior case of Fig. 6 are present again here, this case shows a distinctly different transient result for the air electrode exit nodes (e.g., 57 and 64). This difference will be discussed in more detail below.

5.3. Cross-flow case—load decrease

Results from the cross-flow study examining load decrease dynamics are shown in Figs. 8 and 9. Fig. 8 again shows transient current densities at several node locations on the cell but now for a 0.70–0.77 V load change. The results show a reversed transient as compared to the load increase case as might be expected. In particular, there is a sudden decrease in current flow, which is followed by a gradual increase in current as the temperature of the cell slowly drops allowing the Nernst potential to increase which drives more current. For this case, there is an overall current decrease by a factor of about 0.25.

Fig. 9 shows similar results but for a 0.7–0.957 V load change. These results show an additional feature not seen in the prior results, namely negative current for several nodes over an extended period of time until the cell has reached a new equilibrium state. Here, an overall current decrease by a factor of about 0.87 results.

Finally, Fig. 10 shows a contour plot of the current density for this same case immediately following the load change. As can be seen, a significant portion of the cell experiences this negative current state following the strong load decrease. Close examination of the model data at this time show that the peak negative current density achieved on the cell is about $-1330\ \mathrm{A\,m^{-2}}$. The average cell load current at this time is about $-9\ \mathrm{A\,m^{-2}}$.

5.4. Co-flow case—load decrease

Similar load change cases were studied for the co-flow geometry as for the above counter-flow geometry. Because of the unique results shown under strong load decreases, we present only results for the 0.7–0.957 V load change. The results for the other load change cases in general followed the cross-flow geometry results. Fig. 11 shows a contour plot of the current density immediately following the load change. Again, a significant portion of the cell experiences negative current conditions over a lengthy duration as the cell slowly thermally equilibrates to its new steady state condition. Close examination of the model data at this time show that the

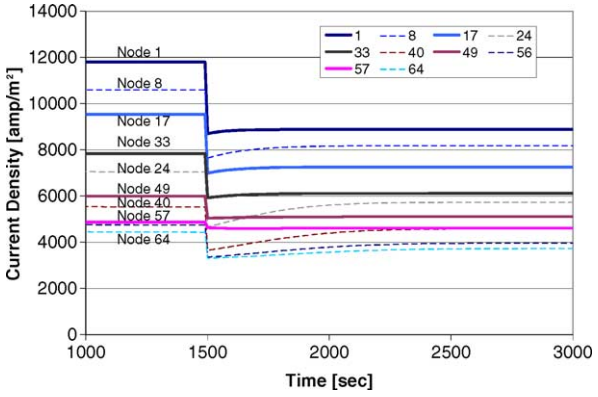

Fig. 8. Cross-flow load decrease (0.7–0.77 V).

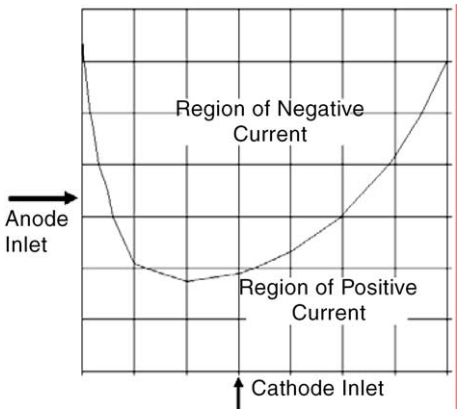

Fig. 10. Contour showing region of current reversal following load decrease (0.70–0.96 V) (cross-flow).

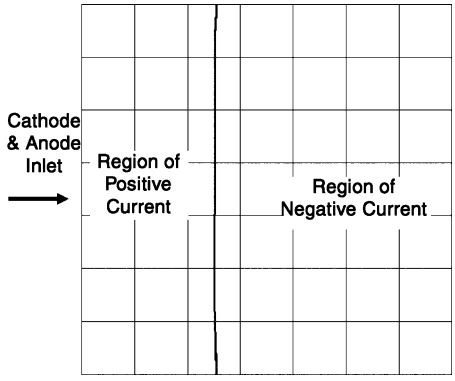

Fig. 11. Contour showing region of current reversal following load decrease (0.70–0.96 V) (co-flow).

peak negative current density achieved on the cell is about $-690\,A\,m^{-2}$. The average cell load current at this time is about $-74\,A\,m^{-2}$.

5.5. Counter-flow case—load decrease

Similar load change cases were again studied for the counter-flow geometry. Again, only results for the 0.7–0.957 V load change are presented. The results for the other load change cases in general followed the cross-flow geometry results. Fig. 12 shows a contour plot of the current density immediately following the load change. Again, a significant portion of the cell experiences negative current conditions over a lengthy duration as the cell slowly thermally equilibrates to its new steady state condition. Close examination of the model data at this time show that the peak negative current density achieved on the cell is about $-1060\,A\,m^{-2}$. The average cell load current density at this time is about $350\,A\,m^{-2}$.

6. Discussion

The results of the button cell and large cell studies are discussed in further detail in the following sections.

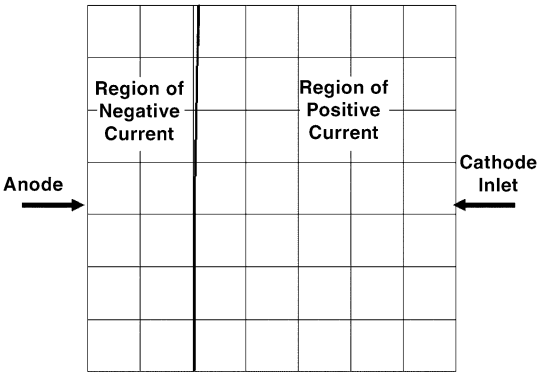

Fig. 12. Contour showing region of current reversal following load decrease (0.70–0.96 V) (counter-flow).

6.1. Button cell case

The close match between model results and experimental data shown in Fig. 5 are encouraging. The need for the slightly different tortuosity/porosity values between the two cases (in order to best match the data) need to be investigated further. Nonetheless, these early results suggest that the model properly accounts for most of the necessary controlling physical issues. It also suggests that the method employed here could be used to help assess some of the important transport parameters of cells. For example, one can perform such high speed transient measurements and then use these models to determine correct values of the parameters that control diffusion, such as effective tortuosity/porosity which are often difficult to assess, especially for thin layers. However, more work needs to be done to determine general validity or applicability. In particular, experimental data on the transient performance of full 10 cm × 10 cm cells would be helpful.

6.2. Cross-flow case

Application of the model to the 10 cm × 10 cm cross-flow geometry shows distinctly different behavior can result depending on the magnitude and direction of a load change. For a small load increase (Fig. 6), all nodes have the same characteristic transient whereby there is a sudden increase in current followed by a gradual decay as the cell equilibrates to its new temperature. On the other hand, for a large load increase (Fig. 7), while most of cell region toward the fuel inlet (e.g., nodes 1, 8, 17 and 24) has a sharp increase in current immediately following a load change, the region toward the fuel exit (e.g., nodes 57 and 64) has a more gradual increase to its peak value. It is also possible to find a certain point in the cell where the controlling effects appear to cancel such that no change in current will occur (e.g., node 49 in Fig. 7).

For a small load decrease (Fig. 8), current at all nodes show largely the same normalized response. However, for large load decrease (Fig. 9), as may occur in an emergency-stop command, certain portions of the cell exhibit current reversal as seen in Fig. 10. The reversed current condition lasts for approximately 330 s for the case studied. It is clear that over this time a certain portion of the cell near the air inlet provides enough current to meet the need of the external load as well as to drive current in reverse over its exit portion. Further analysis of the model data shows that the main driver for this reverse current is the cell thermal non-uniformity. It is found that the air electrode exit portion of the cell results in a lower Nernst potential as compared to that at the inlet. Fig. 13 shows the Nernst potential distribution on the cell immediately following the load decrease. The decreased Nernst voltage at the exit is due to the higher exit temperature (∼100 K higher), and this is enough to drive current in reverse. Based on the first-order analysis for in plane thermal transport, improvements to the model to include such transport would only slightly lessen

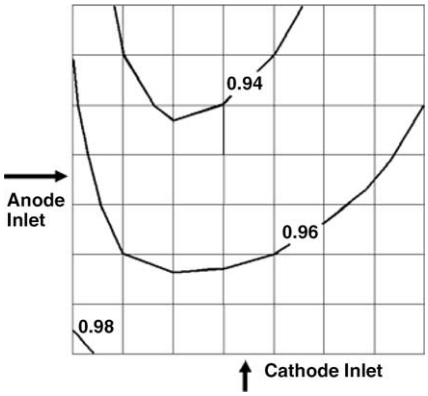

Fig. 13. Contour of Nernst potential following load decrease (0.70–0.96 V) (cross-flow).

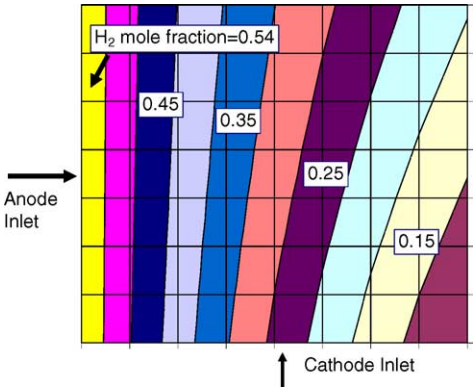

Fig. 15. Hydrogen concentration prior to unload event.

these effects (in both time and magnitude), but will not remove them altogether since the process is thermodynamically driven.

To illustrate what is occurring during current reversal, Fig. 14 shows the path of electric charge through the cell. The left portion of the cell in the figure shows positive current conditions which consume O_2 and H_2 and produce H_2O at the fuel electrode surface. The transferred electrons are provided to the right side of the fuel electrode where H_2O is reduced to generate O^{2-} ions which travel in reverse through the electrolyte to generate O_2 at the air electrode. The electrons released on the right side of the air electrode traverse back to the left portion of the cell and the process continues until the thermodynamic driving potential no longer exists to drive this process. As a check for consistency in the numeric calculation, Figs. 15 and 16 show the hydrogen concentration that results just prior to and after the unload event, respectively. On the whole, Fig. 15 shows a gradual decay in hydrogen concentration as the fuel electrode flow passes through the cell, as expected. Fig. 16 shows a near recovery of the hydrogen concentration to values close to the supply concentration ($y_{H_2} = 0.54$), as would be expected for an unload event. However, they are modified slightly by the consumption of hydrogen toward the air electrode inlet, and the creation of hydrogen at the air electrode exit (per the current density field shown in Fig. 10). The self-consistency of these results confirms that the current reversal identified is not likely due to some anomalous numerical computation.

6.3. Co-flow, counter-flow and cross-flow comparison

The temperature profile has been identified as the governing driving method for the reverse current following load decrease. As such, the CoF and CtF results can be expected to be different from the CrF results, and follow the thermal characteristics of those designs. This result is clearly evident in the current density contours shown in Figs. 11 and 12 for the CoF and CtF cases, respectively. Past work by others, Khaleel et al. [25], have already shown that CtF, CrF, and CoF geometries result in different temperature variations over the cell, $dT/T = 0.352, 0.349, 0.241$, respectively. The results here for current reversal are consistent with these thermal results whereby the CtF, CrF and CoF geometries show a current reversal from the average current ($R = \mathrm{Min}(i) - \mathrm{Ave}(i)$) as -1410, -1321, $-616\ \mathrm{A\,m^{-2}}$, respectively. It is apparent that the overall temperature difference is a sufficient indicator for predicting the presence of current reversal during high unload events.

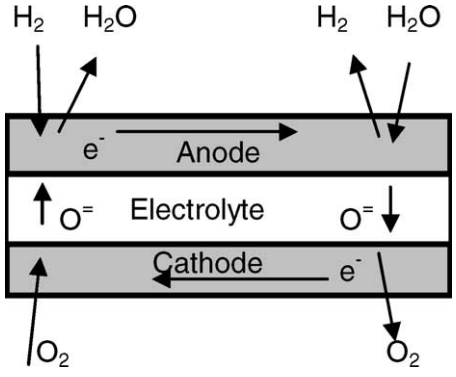

Fig. 14. Schematic representation of electron charge path occurring during reverse current.

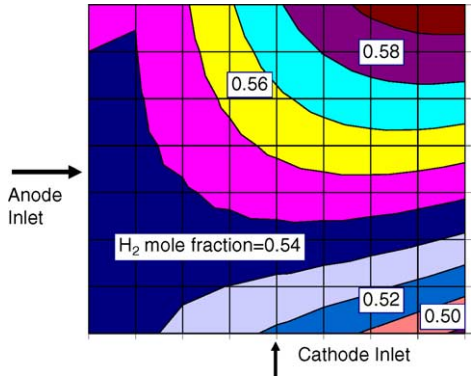

Fig. 16. Hydrogen concentration after unload event.

The aforementioned cases all employed a 0.7–0.957 V load change. The model was implemented a second time for each geometry to determine the acceptable limit of load variation (in terms of current) that would avoid the current reversal conditions. For the CrF, CoF and CtF geometries, the limit of load current decrease was 83, 85 and 86%, respectively, from their full load cell voltage condition of 0.7 V. Load changes that would induce a greater decrease in cell load current will cause at least some portion of the cell to produce reversed current.

The reverse current conditions identified by the model have not been described previously, and more work is needed to examine the limiting conditions where such reversal occurs. If such conditions are indeed found to be possible for a given fuel cell system, then the SOFC system designer may need to consider its impact on the cell components. For example, it is not yet clear if the thermodynamic potential that drives this current reversal will result in material degradation. In an emergency shutdown, for instance, the external load is disconnected and fuel supply shut off. As long as the internal thermodynamic driving potential exists to support internal reverse current, then certain portions of the cell may be exposed to very different reactant concentrations from what is present during normal operation. For example, higher oxygen activity may be produced at points on the fuel electrode having positive current which is supporting the negative current driven elsewhere. Clearly, more work is needed to help assess the true impact to a cell from these conditions.

7. Conclusions

This paper examines the effect of load transients on cells. Results from both experiments and modeling are compared to assess the ability of the model to represent fuel cell operation. Satisfactory comparisons are found between the data and the model. The model is then applied to three planar geometries presently being considered by industry (co-flow, counter-flow and cross-flow) to develop improved understanding of how SOFC fuel cells respond to various real-world upset conditions. Of particular note are results showing load-decrease cases having reverse current over significant portions of the cell, starting from the moment of load perturbation up to the point where equilibrated conditions again provide positive current. Such reverse current conditions arise for all geometry types studied, although the cross-flow case is more severe for the same magnitude of load change. An estimate of the load change limit such that negative current conditions are avoided is 80–85%. Any load decrease greater than this will cause current reversal over at least portions of the cell. It is suggested that conditions for current reversal be examined further given the potential risk for electrode degradation, especially in cases of emergency shut-down when fuel is often removed from the cell.

Acknowledgement

The authors wish to thank Mr. Neil Buzzard for his help with executing the model and model analysis.

References

[1] W.A. Surdoval, S.C. Singhal, G.L. McVay, Presented at the 7th International Symposium on Solid Oxide Fuel Cells, Tsukuba, Japan, June 3–8, 2001.
[2] V. Acquaviva, P. Poggi, M. Muselli, A. Louche, Energy 25 (2002) 741–756.
[3] E.A. Liese, R.S. Gemmen, F. Jabbari, J. Brouwer, Proceedings of the ASME Turbo Expo 1999, Indianapolis, IN, 1999.
[4] M.D. Lukas, K.Y. Lee, H. Ghezel-Ayagh, Proceedings of the IEEE Transactions on Energy Conversion, PE-468-EC-0-01-1999, 1999.
[5] P. Costamagna, L. Magistri, A.F. Massardo, J. Power Sources 96 (2000) 352–368.
[6] S. Kimijima, N. Kasagi, Proceedings of the ASME Turbo Expo 2002, GT-2002-30111, Amsterdam, The Netherlands, June 3–6, 2002.
[7] J. Padulles, G.W. Ault, J.R. McDonald, J. Power Sources 86 (2000) 495–500.
[8] E. Achenbach, J. Power Sources 57 (1995) 105–109.
[9] C. Haynes, J. Power Sources 109 (2002) 365–376.
[10] T. Ota, M. Koyama, C. Wen, K. Yamada, H. Takahashi, J. Power Sources 118 (2003) 430–439.
[11] P. Hensel, R. Gemmen, B. Hetzer, J. Thornton, J. Vipperman, W. Clark, A.F. Ayhan, Proceedings of the 2004 Conference on Fuel Cell Science, Engineering and Technology, Rochester, New York, June 14–16, Paper No. FUELCELL2004-2482, 2004, pp. 283–290.
[12] R.S. Gemmen, E. Liese, J.G. Rivera, F. Jabbari, J. Brouwer, Proceedings of the ASME Turbo Expo 2000, 2000-GT-0554, Munich, Germany, 2000.
[13] S. Ahmed, C. McPheeters, R. Kumar, Electrochem. Soc. 138 (9) (1991) 2712–2718.
[14] S. Chen, J. Evans, J. Power Sources 58 (1996) 87–91.
[15] S. Srinivasan, A.V. Omourtag, A. Parthasarathy, D.J. Manko, A.J. Appleby, J. Power Sources 36 (1991) 299–320.
[16] V. Arpaci, P. Larsen, Convective Heat Transfer, Prentice-Hall, New Jersey, 1984.
[17] S. Srinivasan, B. Dave, K. Murugesamoorthi, A. Parthasarathy, A. Appleby, in: L.J.M.J. Blomen, M.N. Mugerwa (Eds.), Fuel Cell Systems, Plenum Press, New York, 1993, pp. 37–72.
[18] J. Hirschenhofer, D. Stauffer, R. Engleman, Fuel Cells—A Handbook, Revision 3, DOE/METC-94/1006, 1994.
[19] R.S. Gemmen, P. Famouri, C. Johnson, Proceedings of the ASME First International Conference on Fuel Cell Science, Engineering and Technology, Rochester, New York, USA, April 21–23, 2003, Paper No. FUELCELL2003-1744, 2003.
[20] E. Barendrecht, in: L.J.M.J. Blomen, M.N. Mugerwa (Eds.), Fuel Cell Systems, Plenum Press, New York, 1993, pp. 73–119.
[21] S.B. Adler, J.R. Wilson, D.T. Schwartz, in: S.C. Singhal, M. Dokiya (Eds.), Solid Oxide Fuel Cells. VIII. Electrochemical Society Proceedings, 2003-07, 2003, pp. 516–524.
[22] M.G.H.M. Hendriks, J.E. ten Elshof, H.J.M. Bouwmeester, H. Verweij, Solid State Ionics 146 (2002) 211–217.
[23] S.V. Patankar, Numerical Heat Transfer and Fluid Flow, Hemisphere Publishing Corp., New York, 1980.
[24] R.A. Roberts, J. Brouwer, R.S. Gemmen, E. Liese, Proceedings of the ASME Turbo Expo 2003, GT2003-38774, Atlanta, GA, 2003.
[25] M. Khaleel, K. Recknagle, D. Rector, J. Deibler, R. Pagh, R. Williford, L. Chick, Proceedings of the SECA Core Technology Review Meeting, Pittsburgh, PA, June 19, 2002.